Magnetoplasmons for Ultrasensitive Label-Free Biosensing

Sayan Chandra, Jared Cozart, Aritra Biswas, Sang Lee, and Debashis Chanda*

Cite This: *ACS Photonics* 2021, 8, 1316–1323

Read Online

ACCESS | Metrics & More | Article Recommendations | SI Supporting Information

ABSTRACT: Early detection of immunoglobin G (IgG), a glycoprotein antibody produced in the serum due to various infections, is of paramount importance that will enable effective treatment, immunity assessment, and assist in monitoring outbreaks of contagious diseases. This work demonstrates the transverse magneto-optic Kerr effect (T-MOKE) based magnetoplasmons excited on a composite ferromagnetic/plasmonic grating as a highly sensitive, single wavelength, and target specific biosensing platform. The sharp T-MOKE sensitivity curve corresponding to reduced fwhm results in a two orders of magnitude enhancement in the resolving power compared to conventional propagating surface plasmon polariton (SPP), which is pivotal in identifying minute fluctuations in specific biomolecular concentrations. An order of magnitude improvement in antibody immunoglobin G (IgG) detection limit is observed compared to the SPP based sensing. A detection limit down to 10 ng/mL (66 pM) is achieved using the proposed T-MOKE technique. The results obtained provide compelling evidence of the significantly superior sensitivity and resolving power of the T-MOKE technique for the detection of Human IgG, and it is envisioned that this spectroscopy free, single wavelength measurement approach can be extended to detect biologically/chemically relevant molecules at lower concentrations for early biomedical diagnosis and therapy.

**KEYWORDS:** *immunoglobin G, magnetoplasmonics, label-free detection, biosensing, nanoimprinting*
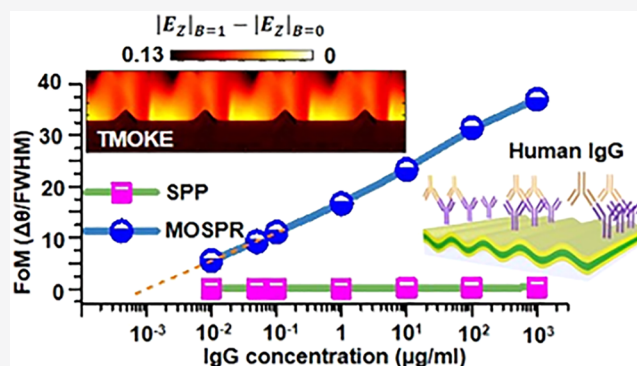
Biomolecule sensing has been an area of intensive research over the past decades and has fundamentally revolutionized medical diagnosis and therapy.[1−4] Currently, the pressing objective for biomolecule sensing is to develop techniques that offer higher sensitivity, lower false positive, and high throughput.[5−10] This enables rapid early detection of biomolecules (for example, antibody), which is critical to prevent outbreaks of infectious diseases like SARS-CoV-2.[11−13] Immunoglobin G (IgG) is one such antibody found in our blood that is produced because of an infection as a secondary immune response.[14−17] Detection of IgG is also a crucial component for determining evaluations of allergies and autoimmune disorders. While the total concentration of IgG found in the adult plasma is about 7 mg/mL,[18] IgG antibodies generated from different infections have significantly lower concentrations at the onset and exhibit unique chemical signatures.[19] This underscores the need for an infection specific detection of IgG at low concentrations with high sensitivity.[20−23] Conventionally, antibody detection is done using the techniques like polymerase chain reaction (PCR), enzyme-linked immunosorbent assay (ELISA), or Western blot that are reliable, however, they are time-consuming processes, prone to contamination, and require high volumes of samples for definitive evaluation.[24−27] Alternatively, optical techniques for detection of biomolecules offer the benefits of faster sensing

and can be done using a fraction of the sample quantity.[28−34] With label-free detection, the concerns of affecting antibody binding affinities and introducing undesired interactions or modifications is eliminated. This removes the restrictions that tag labels such as dyes give, where it can only see the binding at the very end or can potentially modify the sample outside of its' natural state.

Optical sensing techniques utilize fiber Bragg gratings, whispering gallery modes, plasmonics as various platforms for detection.[35−39] Both localized (LSP) and propagating surface plasmons (SPP) have been investigated for sensing,[40,41] with comparable sensitivity to single-molecule binding events.[39] This is primarily due to the relatively sharp SPP resonance bandwidth and phase-matching requirements. Fluctuations in the surrounding refractive index changes the phase-matching condition and subsequently the resonance peak shifts. By coupling a magnetic material to the plasmonic systems, the combined magneto-optic properties result in the generation of
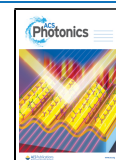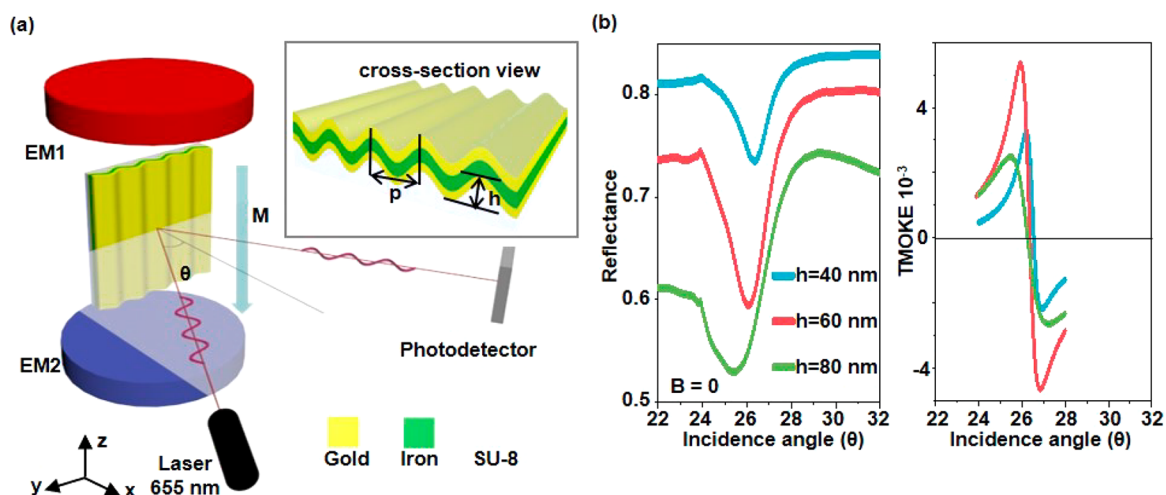
Figure 1. Transverse magneto-optic Kerr effect. (a) Schematic representation of the magneto-optic sensor platform. (b) Effect of grating height on the specular reflectance (left) and T-MOKE (right), as obtained from FDTD simulations.
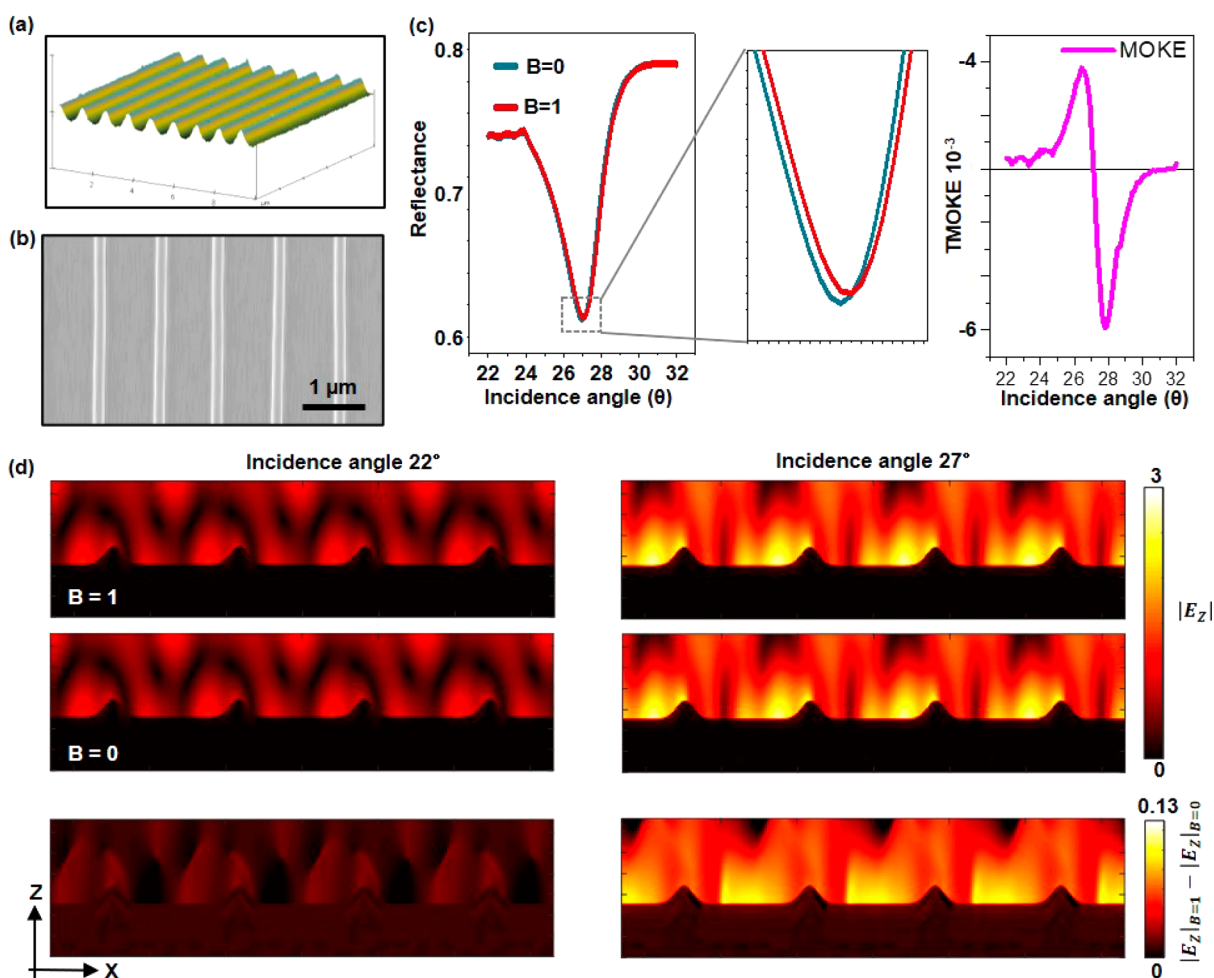

Figure 2. T-MOKE optimization. (a) 3D reconstruction of AFM image of the nanoimprinted grating surface and (b) SEM image of the fabricated samples with 60 nm grating height. (c) SPP curves as a function of angle of incidence with and without magnetic field. Middle panel shows magnified image. Right panel shows the calculated T-MOKE signal from the SPP curves. (d) Out-of-plane electric field profile at 22° (left) and 27° (right) angle of incidence for cases $B = 1$ (top), $B = 0$ (middle), and their difference (bottom)

magnetoplasmons under special circumstances that can be used as a probe to detect a very low concentration of biomolecules.[42−48] The sensing properties and magneto-optical activity are yet to be fully explored in comparison to

conventional SPP sensing platforms. Typically, Kretschman geometry[49,50] is implemented to excite SPP on a noble metal that is layered with a soft ferromagnet and optically coupled to a prism to produce magnetoplasmons, which makes the sensor

configuration bulky.[51] On the other hand, it is possible to excite SPP assisted magnetoplasmons on grating surfaces by sandwiching a ferromagnetic material in the thin-film grating stack that are highly compact.[42,52−54] In this work, for the first time we demonstrate an ultrasensitive magneto surface plasmon resonance (MOSPR) based direct detection of IgG antibody. We implement the transverse magneto optic Kerr effect (T-MOKE) for MOSPR generation on a trimetal Au/Fe/Au layered 1D grating. The appeal of the transverse geometry lies in the simplicity of the optical setup, where we track the angular response of the intensity of the single wavelength reflected light ($\lambda = 655$ nm), eliminating the need of spectroscopic measurement. We demonstrate that by using the MOSPR technique, we can improve sensitivity by two orders of magnitude and attain a one order lower detection limit than what is achievable using traditional SPP.

Figure 1a shows a schematic of the transverse magneto-optic Kerr measurement setup. The functionalized 1D grating surface is placed between two electromagnets such that the grating lines are parallel to the direction of the magnetic field. The magnetoplasmons are excited on a Au/Fe/Au trilayer structure where an iron layer that is sandwiched between two gold layers. A p-polarized 655 nm laser is incident on the sample and the zeroth order light reflected from the sample is measured using a silicon detector. In the apparatus, the detector is stationary while the sample and laser rotate by θ and 2θ, respectively for the goniometric measurement. In order to improve the signal-to-noise ratio, the incident light is modulated at a fixed frequency (1167 Hz) and the signal from the silicon detector is measured using a lock-in-detector. The 1D grating surface is fabricated based on a simple nano-imprinting technique. A large area (4×4 mm^2) master 1D grating pattern was written using direct laser lithography on an ITO-coated glass slide. Following this, a PDMS stamp was prepared from the master, which was used as a mold for nanoimprinting the 1D grating surface on a 150 nm thick SU-8 polymer film spin coated on a glass slide. Subsequently, the trilayer bottom-Au (50 nm)/Fe (20 nm)/top-Au (35 nm) was electron-beam evaporated on the grating surface to complete the sample fabrication. In order to excite propagating surface plasmons (SPP) on the dielectric-metal interface the period of the grating was chosen such that the energy and momentum wave vector of the incident light is conserved and equals the plasmon wave vector as eq 1.

$$\frac{2\pi}{\lambda}\sqrt{\frac{\varepsilon_m(\lambda)n_i^2}{\varepsilon_m(\lambda) + n_i^2}} = \frac{2\pi}{\lambda}n_i\sin(\theta) + \frac{2\pi}{\lambda}q \quad (1)$$

Here, ε_m and ε_d are the dielectric constants of the metal and dielectric, respectively, θ is the angle of incidence and d is the grating periodicity. For $\varepsilon_d = 1$ for air and $d = 1100$ nm, eq 1 is satisfied when light of $\lambda = 655$ nm is incident at 26° for diffraction order $n = 1$. Figure 2a,b shows the 3D rendered AFM image of the grating surface and an SEM image for a sample with grating height of 60 nm, respectively. We performed FDTD simulations to investigate the effect of grating height on the line form of the SPP curve as a function of angle of incidence as shown in Figure 1b (left). To make the FDTD predictions accurate, the simulated structure was generated to closely resemble the grating line profile of the fabricated sample as obtained from AFM topography images (Figure 2a). FDTD simulations predict a shallow absorption of ~6% for a grating height of 40 nm, whereas for a grating height

of 80 nm, the line form becomes asymmetric as can be seen in the SI, Figure S2. Therefore, we chose an intermediate grating height of 60 nm that yields a symmetric SPP reflection peak at $\theta = 26°$ with a fwhm of 2° and ~12% absorption.

The dielectric permittivity tensor of the composite Au/Fe/Au layer is given by eq 2. In the absence of magnetic field ($B = 0$), the off-diagonal element $g = 0$. However, when a magnetic field ($B = 1$) is applied along the transverse direction, $g \neq 0$ due to the cross coupling between E and B fields.[42]

$$\varepsilon_{metal} = \begin{pmatrix} \varepsilon_1 & 0 & -ig \\ 0 & \varepsilon_1 & 0 \\ ig & 0 & \varepsilon_1 \end{pmatrix} \quad (2)$$

Here, the off-diagonal terms account for the magneto-optical (MO) response of a material. Due to the weak MO properties of gold, its off-diagonal terms are negligible. However, the complex MO constant of iron[55,56] ($g = -0.25 + i0.625$) has a significant effect on SPP generated on the Au-air interface. As shown in Figure 2c (left), in the presence of the magnetic field, the momentum of the propagating surface plasmons is modified, thereby altering the intensity of the reflected light for a given angle of incidence. This renders a shift in the angle (θ) corresponding to the SPP peak (Figure 2c, middle). Here, we take advantage of the coupling of the excellent plasmonic properties of Au with the strong MO response of the underlying magnetic Fe layer, that is, utilizing magneto-plasmons (MOSPR) for biomolecular sensing. This coupling critically depends on top Au layer thickness. Following the finite difference time domain simulation this coupling is optimized. From Figure S2, we found that top Au layer thickness of 35 nm results in a symmetric T-MOKE signal with enhanced amplitude.

$$\text{T-MOKE} = \frac{R_{pp}(+M) - R_{pp}(-M)}{R_{pp}(+M) + R_{pp}(-M)} \quad (3)$$

By using eq 3, one can quantify the T-MOKE, where R_{pp} is the reflectance of the p-polarized light and $\pm M$ corresponds to the magnetization direction of the Fe layer for $\pm B$ fields, respectively. Equation 3 yields the signature Fano line-shape of the MOSPR curves, as shown in Figure 2c (right). The FDTD simulated T-MOKE curves for different grating heights (Figure 1b, right) show the strongest MOSPR signal for a grating height of 60 nm, which is consistent with the symmetric SPP line form. To elucidate the presence of MOSPR, in Figure 2d, we show the out-of-plane electric field profile for two angles of incidence, (i) 22° and (ii) 27°, which corresponds to the first plasmon resonance angle. In each of these cases, the field profiles for $B = 0$ and $B = 1$ are shown in the top and middle panel. The simulation was done over 4 periods for the better visualization of the electric field. It is evident that the intensity of light coupling at the Au/Air interface at 22° is weak compared to the case of light being incident at 27° where the SPP mode is supported, as per eq 1. The bottom panel shows the field profile corresponding to the MOSPR, which is obtained by taking the difference $|E_Z|_{B=1} - |E_Z|_{B=0}$. This highlights the enhanced T-MOKE signal at 27° arising from the magneto-optic coupling of the SPP, that is, MOSPR at the Au/Air interface of the grating surface.

The evanescent nature of both SPP and MOSPR makes them highly susceptible to changes in the local dielectric constant of the Au/Air interface. We investigated the effect of
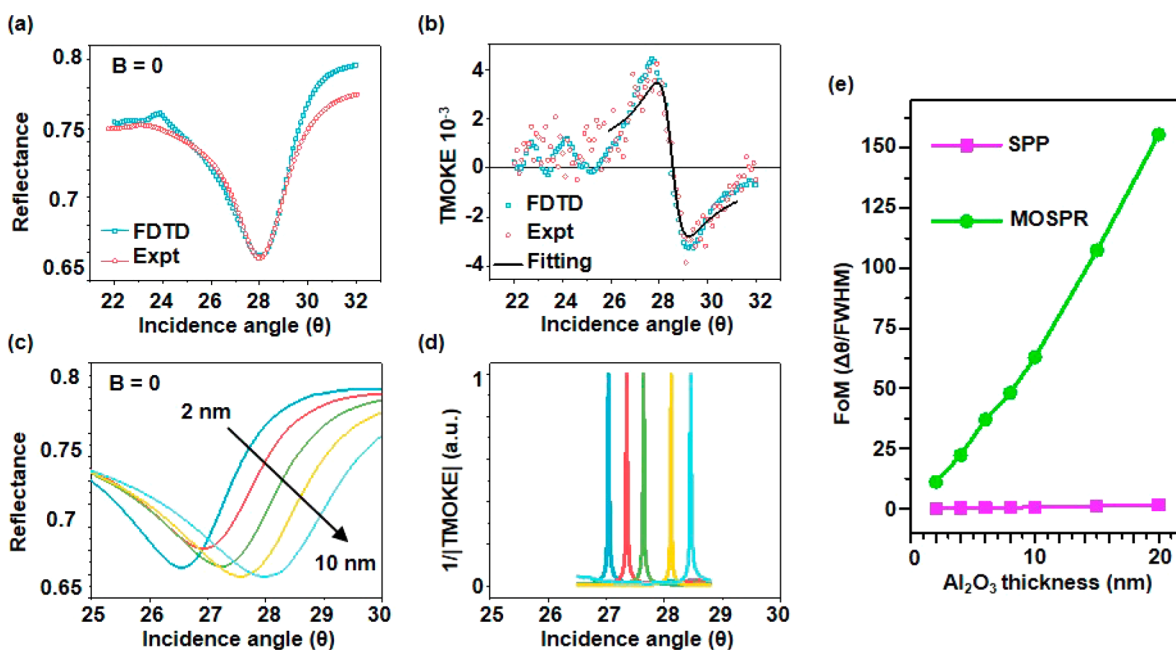
Figure 3. Sensor characterization. Experimental and FDTD simulated (a) SPP and (b) MOSPR curves for 10 nm Al_2O_3 thicknesses. (c) SPP curves and (d) inverse of MOSPR curves as a function of Al_2O_3 thickness. (e) Figure of merit for MOSPR and SPP as a function of Al_2O_3 thickness.
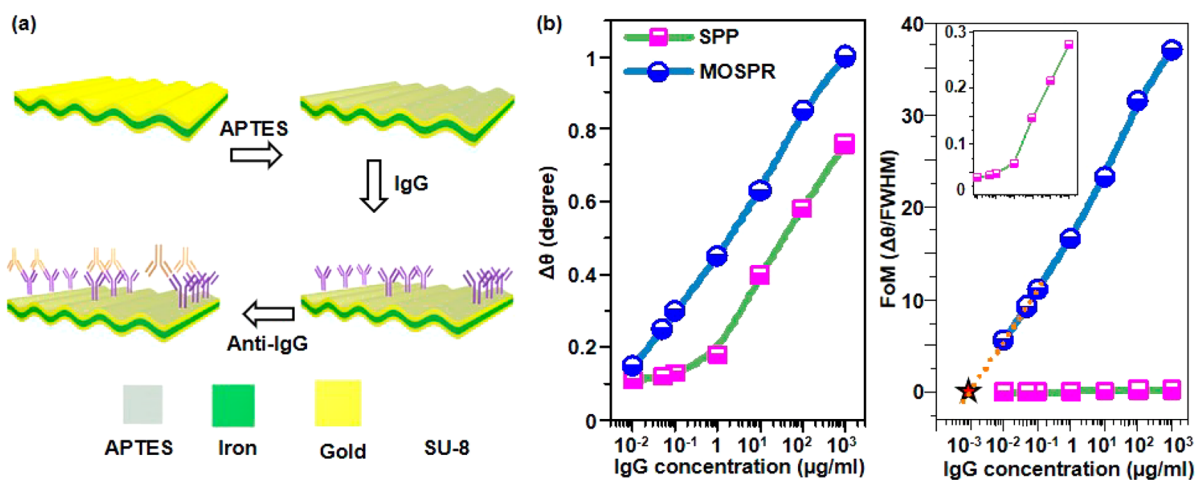

Figure 4. Sensor fabrication. (a) Schematic representation of the biofunctionalization process of the MOKE sensors. (b) Angular shift (left) FoM of SPP and MOSPR peak location (right) as a function of IgG concentration.

varying thickness (2−10 nm) of Al_2O_3 on the samples to characterize the sensitivity of the SPP and MOSPR on the grating surface. Al_2O_3 has a dielectric constant of 8.5 (at $\lambda = 655$ nm); therefore, by gradually increasing the thickness of Al_2O_3, we induce a controlled change in the effective permittivity that the incident light experiences, which manifests as a shift in the peak location from that of the bare sample. For this study, we used a sample with a grating height of 60 nm, and before every measurement, an additional 2 nm Al_2O_3 layer was deposited by ALD until the total thickness was 10 nm. The Al_2O_3 deposition was done at 80 °C to prevent the grating surface from being deformed due to thermal deformation in the SU-8 polymer layer on which the nanoimprint was done. In Figure 3a, we overlay the FDTD simulated and experimentally measured SPP curves for the sample with 10 nm thick Al_2O_3 layer. We applied a magnetic field of ±240 Oe to saturate the magnetization of the Fe layer (Figure S1) before recording the

SPP curves for respective magnetic orientations. Using eq 3, we calculated the T-MOKE response curves and overlaid them (Figure 3b), thereby exhibiting a reasonably good agreement between simulation and experiment. As the Al_2O_3 thickness is increased, we observe a consistent shift in the SPP peak location from 26.6° for the bare sample to 28° for a 10 nm Al_2O_3 (Figure 3c). For our analysis, the corresponding T-MOKE response curves for each Al_2O_3 thickness were calculated and fitted to a Fano line form, as shown in Figure 3b. Therefore, we obtain the precise angle at which the T-MOKE signal changes sign, associated with the crossover of the two SPP curves, obtained from the ±B. We attribute the shift in the angular location of the crossover point to the sensitivity of the MOSPR to a varying effective index of refraction. This crossover point can be better visualized by simply taking the inverse of the magnitude of the T-MOKE signal, as shown in Figure 3d. Consequently, the MOSPR

response curve appears as a sharp peak with a fwhm that is determined by the slope of the T-MOKE signal (Figure 2b) near the crossover point.

Generally, the usefulness of a sensor or sensing technique is characterized by its ability to resolve minute changes in a signal. For a sensing technique such as this, where one tracks the relative shift in the location of the peak as a function of angle of incidence $(\Delta\theta)$, the figure of merit (FoM) that represents its resolving power is given by the ratio of $\Delta\theta$ to the fwhm of the peak function. In other words, the sensing platform with higher FoM = $\Delta\theta$/fwhm offers improved resolution in detecting $\Delta\theta$. Comparing the respective curves for SPP and MOSPR, shown in Figure 3c,d, it is evident that the MOSPR technique yields peaks with a higher Q-factor, resulting in an improvement of FoM over two orders of magnitude compared to conventional SPP (Figure 3e). Therefore, by implementing the T-MOKE technique, we obtain a better resolution in the determining an increase in Al_2O_3 thickness than the conventional SPP method.

Next, we show a comparative study between the two sensing methods (SPP vs MOSPR) for biomolecular detection, namely, human IgG. The grating sample was treated for functionalization using a technique similar to that reported earlier[41,57−59] and described in the SI for the present context. We prepared several samples with varying concentrations of secondary IgG antibody from 10 ng/mL (66 pM) to 1 mg/mL (6.6 μM; Figure S3). In Figure 4b (left) we show the evolution of the peak location as a function of IgG concentration for both SPP and MOSPR sensing methods. We studied samples with seven concentrations of anti-IgG to obtain Figure 4b, with the objective to compare the sensitivity of the SPP and MOSPR techniques. This is in good agreement with other reports where it is seen that the MOSPR exhibits overall higher $\Delta\theta$ than SPP for a given change in the concentration.[48] While both show an appreciable peak shift for higher concentrations, below 100 ng/mL, we find that the slope of the $\Delta\theta$ versus IgG concentration curve for SPP distinctly drops, thereby establishing that, at lower concentration changes, the MOSPR technique is superior. The resolving power of the two techniques is expressed in Figure 4b (right). Consistent with our study on varying Al_2O_3 thicknesses, we find that the MOSPR technique offers a two-order improvement in resolving changes in the human IgG concentration. For better visualization of the FoM for the SPP technique, we provide a magnified image in the inset. Although the FoM for SPP is responsive to different concentrations down to 66 pM, the diminishing detection limit of this technique is evident by the reduced slope of the curve below FoM of 0.1. On the other hand, the FoM for the MOSPR curve retains the same slope as a function of concentration down to 66 pM. Therefore, for a consistent comparison with the SPP technique, we extrapolate the MOSPR curve (as shown) along the y-axis to a FoM of 0.1, signifying the detection limit of a technique. We estimate the limit of detection for the MOSPR technique to be 1 ng/mL (6.6 pM) associated with a FoM of 0.1. We did not decrease the concentration below 10 ng/mL because the sensitivity of the SPP technique is lost, and therefore, a comparison between the SPP and MOSPR techniques was not possible at a concentration of 1 ng/mL. Furthermore, by taking advantage of the label-free detection process, direct detection of biomolecules from plasma can be easily achieved through the integration of microfluidic channels onto the sensor, as demonstrated in our previous work.[33]

CONCLUSION

In conclusion, we have demonstrated a remarkable enhancement in sensitivity of biomolecule detection using magnetoplasmons. The appeal of the technique lies in the simplicity of the optical setup, where we track the angular response of the intensity of the single wavelength reflected light, eliminating the need for spectroscopic measurement, which is a bottleneck for low cost, high-throughput biosensing. We show that, by using the MOSPR technique, we can improve sensitivity by two orders of magnitude and attain one order improvement in the detection limit than what is achievable using traditional SPP. This is established by demonstrating the lower detection limit of the IgG antibody molecule. For the same FoM of 0.1, the lowest detection limit of T-MOKE is ∼1 ng/mL (6.6 pM), which is an order improvement over the conventional SPP technique with a detection limit of 10 ng/mL (66pM). While this study focuses on a human IgG, the single wavelength T-MOKE sensors can be implemented for high-resolution sensing of other biomolecules, gases, and chemical entities based on an imprinted simple 1D grating platform without needing expensive spectrometers.

EXPERIMENTAL SECTION

Functionalization of the Sensor. The grating sample was treated for functionalization as follows. First, (3-aminopropyl) triethoxysilane (APTES) solution used to immobilize the immunoglobulin G (IgG) antibodies was prepared.[41,57−59] The solution consisted of 1.9 mL of pure ethyl alcohol, 0.1 mL of APTES, and 0.1 mL of DI water. The APTES and DI water were added slowly, drop by drop, to prevent the APTES from precipitating. This mixture was stirred on a hot plate for 2 h at 700 rpm and then diluted by adding 100 μL of APTES solution to 900 μL of regular ethyl alcohol. Thereafter, 0.15 mL of the new solution was added to 1.35 mL of regular ethyl alcohol. Prior to the application of the APTES solution, the patterned samples were cleaned with ethanol and water, dried with nitrogen, and then cleaned with an oxygen plasma. After the samples were cleaned, they were each covered in 150 μL of APTES solution and then allowed to incubate for 1 h at room temperature. After incubation, the excess APTES solution was rinsed with water and dried in nitrogen. The samples were then baked on a hot plate for 1 h at 80 °C. During this 1 h bake, the primary antibody solution was prepared by diluting anti-human IgG in a phosphate-buffered saline solution (PBS). The diluted primary antibody solution was then mixed with 4 mg/mL of EDC in a 99:1 ratio for 15 min at 37 °C to enable coupling activation. Once the baking was finished, 12 μL of the primary antibody solution was added to the samples. Polydimethylsiloxane (PDMS) wells were used to keep the antibody solution on the pattern. After the primary antibody solution was added, the samples were set in an oven to incubate for 1 h at 37 °C. During this time, the secondary antibody solution was prepared by diluting human IgG in PBS. After the primary antibody solution has finished incubating, excess solution is cleaned off with a rinse of PBS and then water. Excess water is sucked out of the PDMS well with first a pipet and then by an absorbent cloth. After drying, 12 μL of the secondary antibody solution was added into the same PDMS well. The samples were then incubated at room temperature for 1 h. After incubation, the excess secondary antibody solution was cleaned by gently submerging the sample into PBS and water instead of

a rinse (Figure 4a). Following this, the samples were dried under ambient conditions.

Direct Laser Lithography. Masters for the nanoimprint lithography process were created by direct laser writing using a Nanoscribe GT (Nanoscribe, GmbH) equipped with a galvo scanner. A negative photoresin, IP-Dip was drop-casted on an ITO-coated glass slide to perform the direct laser write. Following the write process, the master was developed in propylene glycol monomethyl ether acetate (PGMEA, Sigma-Aldrich) for 20 min and then in IPA for 2 min. Variations in line width and relief depth of the grating were optimized by adjusting the intensity of the exposing beam and voxel height with respect to the surface of the substrate.

FDTD Modeling. FDTD simulations of the grating to investigate the SPR and MOSPR were done using a commercial software package (Lumerical FDTD, Lumerical Solutions Inc.).

■ ASSOCIATED CONTENT

ⓢ Supporting Information

The Supporting Information is available free of charge at https://pubs.acs.org/doi/10.1021/acsphotonics.0c01646.

Three supporting figures with captions (PDF)

■ AUTHOR INFORMATION

Corresponding Author

Debashis Chanda − *NanoScience Technology Center, University of Central Florida, Orlando, Florida 32826, United States; CREOL, The College of Optics and Photonics and Department of Physics, University of Central Florida, Orlando, Florida 32816, United States;*
Email: debashis.chanda@ucf.edu

Authors

Sayan Chandra − *NanoScience Technology Center, University of Central Florida, Orlando, Florida 32826, United States; Department of Physics and Astronomy, Appalachian State University, Boone, North Carolina 28608, United States*

Jared Cozart − *CREOL, The College of Optics and Photonics, University of Central Florida, Orlando, Florida 32816, United States*

Aritra Biswas − *CREOL, The College of Optics and Photonics, University of Central Florida, Orlando, Florida 32816, United States*

Sang Lee − *NanoScience Technology Center, University of Central Florida, Orlando, Florida 32826, United States*

Complete contact information is available at:
https://pubs.acs.org/10.1021/acsphotonics.0c01646

Author Contributions

S.C. conceived the idea and designed the experiments. J.C. and S.C. fabricated the samples and conducted the measurements. S.C., J.C., A.B., and S.L. functionalized the sensors with antibody. S.C. and D.C. analyzed the data. D.C. provided resources. S.C. and D.C. cowrote the manuscript.

Notes

The authors declare no competing financial interest.

■ ACKNOWLEDGMENTS

■ REFERENCES

(1) Chen, C.; Wang, J. S. Optical biosensors: an exhaustive and comprehensive review. *Analyst* **2020**, *145* (5), 1605−1628.

(2) Fan, X. D.; White, I. M.; Shopova, S. I.; Zhu, H. Y.; Suter, J. D.; Sun, Y. Z. Sensitive optical biosensors for unlabeled targets: A review. *Anal. Chim. Acta* **2008**, *620* (1−2), 8−26.

(3) Borisov, S. M.; Wolfbeis, O. S. Optical biosensors. *Chem. Rev.* **2008**, *108* (2), 423−461.

(4) Sharma, S.; Kumari, R.; Varshney, S. K.; Lahiri, B. Optical biosensing with electromagnetic nanostructures. *Reviews in Physics* **2020**, *5*, 100044.

(5) Dervisevic, M.; Alba, M.; Prieto-Simon, B.; Voelcker, N. H. Skin in the diagnostics game: Wearable biosensor nano- and microsystems for medical diagnostics. *Nano Today* **2020**, *30*, 100828.

(6) Lei, Y.; Zhao, W.; Zhang, Y.; Jiang, Q.; He, J.-H.; Baeumner, A. J.; Wolfbeis, O. S.; Wang, Z. L.; Salama, K. N.; Alshareef, H. N. A MXene-Based Wearable Biosensor System for High-Performance In Vitro Perspiration Analysis. *Small* **2019**, *15* (19), 1901190.

(7) Kim, J.; Sempionatto, J. R.; Imani, S.; Hartel, M. C.; Barfidokht, A.; Tang, G. D.; Campbell, A. S.; Mercier, P. P.; Wang, J. Simultaneous Monitoring of Sweat and Interstitial Fluid Using a Single Wearable Biosensor Platform. *Adv. Sci.* **2018**, *5* (10), 1800880.

(8) Kim, J.; Campbell, A. S.; de Avila, B. E. F.; Wang, J. Wearable biosensors for healthcare monitoring. *Nat. Biotechnol.* **2019**, *37* (4), 389−406.

(9) Vigneshvar, S.; Sudhakumari, C. C.; Senthilkumaran, B.; Prakash, H. Recent Advances in Biosensor Technology for Potential Applications - An Overview. *Front. Bioeng. Biotechnol.* **2016**, *4*, 11.

(10) Abreu, C. M.; Soares-dos-Reis, R.; Melo, P. N.; Relvas, J. B.; Guimaraes, J.; Sa, M. J.; Cruz, A. P.; Pinto, I. M. Emerging Biosensing Technologies for Neuroinflammatory and Neurodegenerative Disease Diagnostics. *Front. Mol. Neurosci.* **2018**, *11*, 164.

(11) Long, Q. X.; Liu, B. Z.; Deng, H. J.; Wu, G. C.; Deng, K.; Chen, Y. K.; Liao, P.; Qiu, J. F.; Lin, Y.; Cai, X. F.; Wang, D. Q.; Hu, Y.; Ren, J. H.; Tang, N.; Xu, Y. Y.; Yu, L. H.; Mo, Z.; Gong, F.; Zhang, X. L.; Tian, W. G.; Hu, L.; Zhang, X. X.; Xiang, J. L.; Du, H. X.; Liu, H. W.; Lang, C. H.; Luo, X. H.; Wu, S. B.; Cui, X. P.; Zhou, Z.; Zhu, M. M.; Wang, J.; Xue, C. J.; Li, X. F.; Wang, L.; Li, Z. J.; Wang, K.; Niu, C. C.; Yang, Q. J.; Tang, X. J.; Zhang, Y.; Liu, X. M.; Li, J. J.; Zhang, D. C.; Zhang, F.; Liu, P.; Yuan, J.; Li, Q.; Hu, J. L.; Chen, J.; Huang, A. L. Antibody responses to SARS-CoV-2 in patients with COVID-19. *Nat. Med.* **2020**, *26* (6), 845.

(12) Chen, Z. H.; Zhang, Z. G.; Zhai, X. M.; Li, Y. Y.; Lin, L.; Zhao, H.; Bian, L.; Li, P.; Yu, L.; Wu, Y. S.; Lin, G. F. Rapid and Sensitive Detection of anti-SARS-CoV-2 IgG, Using Lanthanide-Doped Nanoparticles-Based Lateral Flow Immunoassay. *Anal. Chem.* **2020**, *92* (10), 7226−7231.

(13) Hou, H. Y.; Wang, T.; Zhang, B.; Luo, Y.; Mao, L.; Wang, F.; Wu, S. J.; Sun, Z. Y. Detection of IgM and IgG antibodies in patients with coronavirus disease 2019. *Clin. Transl. Immunol.* **2020**, *9* (5), No. e1136.

(14) Vidarsson, G.; Dekkers, G.; Rispens, T. IgG subclasses and allotypes: from structure to effector functions. *Front. Immunol.* **2014**, *5*, 520.

(15) Schwab, I.; Nimmerjahn, F. Intravenous immunoglobulin therapy: how does IgG modulate the immune system? *Nat. Rev. Immunol.* **2013**, *13* (3), 176−189.

(16) Isa, M. B.; Martinez, L.; Giordano, M.; Zapata, M.; Passeggi, C.; De Wolff, M. C.; Nates, S. Measles virus-specific immunoglobulin G isotype immune response in early and late infections. *J. Clin. Microbiol.* **2001**, *39* (1), 170−174.

(17) Krammer, F. The human antibody response to influenza A virus infection and vaccination. *Nat. Rev. Immunol.* **2019**, *19* (6), 383−397.

(18) Gonzalez-Quintela, A.; Alende, R.; Gude, F.; Campos, J.; Rey, J.; Meijide, L. M.; Fernandez-Merino, C.; Vidal, C. Serum levels of immunoglobulins (IgG, IgA, IgM) in a general adult population and

their relationship with alcohol consumption, smoking and common metabolic abnormalities. *Clin. Exp. Immunol.* **2008**, *151* (1), 42−50.

(19) Schroeder, H. W.; Cavacini, L. Structure and function of immunoglobulins. *J. Allergy Clin. Immunol.* **2010**, *125* (2), S41−S52.

(20) Desbois, D.; Grangeot-Keros, L.; Roquebert, B.; Roque-Afonso, A. M.; Mackiewicz, V.; Poveda, J. D.; Dussaix, E. Usefulness of specific IgG avidity for diagnosis of hepatitis A infection. *Gastroenterol. Clin. Biol.* **2005**, *29* (5), 573−576.

(21) Rasmussen, L.; Kelsall, D.; Nelson, R.; Carney, W.; Hirsch, M.; Winston, D.; Preiksaitis, J.; Merigan, T. C. Virus-Specific Igg and Igm Antibodies in Normal and Immunocompromised Subjects Infected with Cytomegalovirus. *J. Infect. Dis.* **1982**, *145* (2), 191−199.

(22) Scheepers, C.; Chowdhury, S.; Wright, W. S.; Campbell, C. T.; Garrett, N. J.; Karim, Q. A.; Karim, S. S. A.; Moore, P. L.; Gildersleeve, J. C.; Morris, L. Serum glycan-binding IgG antibodies in HIV-1 infection and during the development of broadly neutralizing responses. *AIDS* **2017**, *31* (16), 2199−2209.

(23) Zhao, L. Z.; Hong, W. X.; Wang, J.; Yu, L.; Hu, F. Y.; Qiu, S.; Yin, C. B.; Tang, X. P.; Zhang, L. Q.; Jin, X.; Zhang, F. C. Kinetics of antigen-specific IgM/IgG/IgA antibody responses during Zika virus natural infection in two patients. *J. Med. Virol.* **2019**, *91* (5), 872−876.

(24) Byrne, B.; Stack, E.; Gilmartin, N.; O'Kennedy, R. Antibody-Based Sensors: Principles, Problems and Potential for Detection of Pathogens and Associated Toxins. *Sensors* **2009**, *9* (6), 4407−4445.

(25) Steingart, K. R.; Henry, M.; Laal, S.; Hopewell, P. C.; Ramsay, A.; Menzies, D.; Cunningham, J.; Weldingh, K.; Pai, M. A systematic review of commercial serological antibody detection tests for the diagnosis of extrapulmonary tuberculosis. *Postgrad. Med. J.* **2007**, *83* (985), 705−712.

(26) Niemeyer, C. M.; Adler, M.; Wacker, R. Immuno-PCR: high sensitivity detection of proteins by nucleic acid amplification. *Trends Biotechnol.* **2005**, *23* (4), 208−216.

(27) Waritani, T.; Chang, J.; McKinney, B.; Terato, K. An ELISA protocol to improve the accuracy and reliability of serological antibody assays. *Methodsx* **2017**, *4*, 153−165.

(28) Khansili, N.; Rattu, G.; Krishna, P. M. Label-free optical biosensors for food and biological sensor applications. *Sens. Actuators, B* **2018**, *265*, 35−49.

(29) Dey, D.; Goswami, T. Optical Biosensors: A Revolution Towards Quantum Nanoscale Electronics Device Fabrication. *J. Biomed. Biotechnol.* **2011**, *2011*, 348218.

(30) Duque, T.; Chaves Ribeiro, A. C.; de Camargo, H. S.; Costa Filho, P. A. d.; Mesquita Cavalcante, H. P.; Lopes, D. New Insights on Optical Biosensors: Techniques, Construction and Application. *State of the Art in Biosensors - General Aspects* **2013**, 111−139.

(31) Cooper, M. A. Optical biosensors in drug discovery. *Nat. Rev. Drug Discovery* **2002**, *1* (7), 515−528.

(32) Bertucci, C.; De Simone, A. Optical Biosensors and Applications to Drug Discovery and Development in Cancer Research. *Biosens. Cancer* **2013**, 321−336.

(33) Vazquez-Guardado, A.; Barkam, S.; Peppler, M.; Biswas, A.; Dennis, W.; Das, S.; Seal, S.; Chanda, D. Enzyme-Free Plasmonic Biosensor for Direct Detection of Neurotransmitter Dopamine from Whole Blood. *Nano Lett.* **2019**, *19* (1), 449−454.

(34) Vazquez-Guardado, A.; Smith, A.; Wilson, W.; Ortega, J.; Perez, J. M.; Chanda, D. Hybrid cavity-coupled plasmonic biosensors for low concentration, label-free and selective biomolecular detection. *Opt. Express* **2016**, *24* (22), 25785−25796.

(35) Bekmurzayeva, A.; Dukenbayev, K.; Shaimerdenova, M.; Bekniyazov, I.; Ayupova, T.; Sypabekova, M.; Molardi, C.; Tosi, D. Etched Fiber Bragg Grating Biosensor Functionalized with Aptamers for Detection of Thrombin. *Sensors* **2018**, *18* (12), 4298.

(36) Mejia-Salazar, J. R.; Oliveira, O. N. Plasmonic Biosensing Focus Review. *Chem. Rev.* **2018**, *118* (20), 10617−10625.

(37) Koya, A. N.; Cunha, J.; Guo, T. L.; Toma, A.; Garoli, D.; Wang, T.; Juodkazis, S.; Cojoc, D.; Zaccaria, R. P. Novel Plasmonic Nanocavities for Optical Trapping-Assisted Biosensing Applications. *Adv. Opt. Mater.* **2020**, *8* (7), 1901481.

(38) Sreekanth, K. V.; Dong, W. L.; Ouyang, Q. L.; Sreejith, S.; ElKabbash, M.; Lim, C. T.; Strangi, G.; Yong, K. T.; Simpson, R. E.; Singh, R. Large-Area Silver-Stibnite Nanoporous Plasmonic Films for Label-Free Biosensing. *ACS Appl. Mater. Interfaces* **2018**, *10* (41), 34991−34999.

(39) Sreekanth, K. V.; Alapan, Y.; ElKabbash, M.; Ilker, E.; Hinczewski, M.; Gurkan, U. A.; De Luca, A.; Strangi, G. Extreme sensitivity biosensing platform based on hyperbolic metamaterials. *Nat. Mater.* **2016**, *15* (6), 621.

(40) Roper, D. K.; Ahn, W.; Taylor, B.; Dall'Asen, A. G. Enhanced Spectral Sensing by Electromagnetic Coupling With Localized Surface Plasmons on Subwavelength Structures. *IEEE Sens. J.* **2010**, *10* (3), 531−540.

(41) Lee, K. L.; Hsu, H. Y.; You, M. L.; Chang, C. C.; Pan, M. Y.; Shi, X.; Ueno, K.; Misawa, H.; Wei, P. K. Highly Sensitive Aluminum-Based Biosensors using Tailorable Fano Resonances in Capped Nanostructures. *Sci. Rep.* **2017**, *7*, 44104.

(42) Armelles, G.; Cebollada, A.; Garcia-Martin, A.; Gonzalez, M. U. Magnetoplasmonics: Combining Magnetic and Plasmonic Functionalities. *Adv. Opt. Mater.* **2013**, *1* (1), 10−35.

(43) Armelles, G.; Dmitriev, A. Focus on magnetoplasmonics. *New J. Phys.* **2014**, *16*, 045012.

(44) Jamali, A. A.; Kubler, S.; Muglich, N.; Witzigmann, B.; Ehresmann, A. Electromagnetic study of magneto-optic surface plasmon resonance effects for biosensing applications. *Proc. SPIE* **2013**, 8774.

(45) Faridi, E.; Moradi, M.; Ansari, N.; Ghasemi, A. H. B.; Afshar, A.; Mohseni, S. M. Au/NiFe/M(Au, MoS$_2$, graphene) trilayer magnetoplasmonics DNA-hybridized sensors with high record of sensitivity. *J. Biomed. Opt.* **2017**, *22* (12), 127001.

(46) Moradi, M.; Mohseni, S. M.; Mahmoodi, S.; Rezvani, D.; Ansari, N.; Chung, S.; Akerman, J. Au/NiFe Magnetoplasmonics: Large Enhancement of Magneto-Optical Kerr Effect for Magnetic Field Sensors and Memories. *Electron. Mater. Lett.* **2015**, *11* (3), 440−446.

(47) Maccaferri, N.; Gregorczyk, K. E.; de Oliveira, T. V. A. G.; Kataja, M.; van Dijken, S.; Pirzadeh, Z.; Dmitriev, A.; Akerman, J.; Knez, M.; Vavassori, P. Ultrasensitive and label-free molecular-level detection enabled by light phase control in magnetoplasmonic nanoantennas. *Nat. Commun.* **2015**, *6*, 6150.

(48) Caballero, B.; Garcia-Martin, A.; Cuevas, J. C. Hybrid Magnetoplasmonic Crystals Boost the Performance of Nanohole Arrays as Plasmonic Sensors. *ACS Photonics* **2016**, *3* (2), 203−208.

(49) Ignatyeva, D. O.; Knyazev, G. A.; Kapralov, P. O.; Dietler, G.; Sekatskii, S. K.; Belotelov, V. I. Magneto-optical plasmonic heterostructure with ultranarrow resonance for sensing applications. *Sci. Rep.* **2016**, *6*, 28077.

(50) Lu, H. P.; Liu, C.; Qin, J.; Wang, C. T.; Zhang, Y.; Deng, L. J.; Bi, L. Enhanced magneto-optical Kerr effect and index sensitivity in Au/FexCo1-x magnetoplasmonic transducers. *Photonics Res.* **2017**, *5* (5), 385−390.

(51) Brolo, A. G. Plasmonics for future biosensors. *Nat. Photonics* **2012**, *6* (11), 709−713.

(52) Diaz-Valencia, B. F.; Mejia-Salazar, J. R.; Oliveira, O. N.; Porras-Montenegro, N.; Albella, P. Enhanced Transverse Magneto-Optical Kerr Effect in Magnetoplasmonic Crystals for the Design of Highly Sensitive Plasmonic (Bio) sensing Platforms. *ACS Omega* **2017**, *2* (11), 7682−7685.

(53) Ling, N. P.; Chou, K. H.; Jhou, C. T.; Lai, M. H.; Chen, T. C.; Lai, C. H.; Wang, L. W.; Lee, G. B.; Lee, M. C. M. Observation of Strong Transverse Magneto-Optical Kerr Effect on Surface Plasmonic Gratings. *IEEE Int. Conf. Nano/Micro Eng. Mol. Syst.* **2013**, 653−656.

(54) Chou, K. H.; Lin, E. P.; Chen, T. C.; Lai, C. H.; Wang, L. W.; Chang, K. W.; Lee, G. B.; Lee, M. C. M. Application of strong transverse magneto-optical Kerr effect on high sensitive surface plasmon grating sensors. *Opt. Express* **2014**, *22* (16), 19794−19802.

(55) Krinchik, G. S.; Artemev, V. A. Magneto-Optical Properties of Ni,Co,and Fe in Ultraviolet Visible and Infrared Parts of Spectrum. *J. Exp. Theor. Phys.* **1968**, *26* (6), 1080.

(56) Delin, A.; Eriksson, O.; Johansson, B.; Auluck, S.; Wills, J. M. Calculated magneto-optical properties of cubic and tetragonal Fe, Co, and Ni. *Phys. Rev. B: Condens. Matter Mater. Phys.* **1999**, *60* (20), 14105−14114.

(57) Dixit, C. K.; Vashist, S. K.; MacCraith, B. D.; O'Kennedy, R. Multisubstrate-compatible ELISA procedures for rapid and high-sensitivity immunoassays. *Nat. Protoc.* **2011**, *6* (4), 439−445.

(58) Jadhav, S. A. Self-assembled monolayers (SAMs) of carboxylic acids: an overview. *Cent. Eur. J. Chem.* **2011**, *9* (3), 369−378.

(59) Majoul, N.; Rasson, J.; Francis, L. A.; Aouida, S.; Bessais, B. Immobilization of hydroxocobalamin (vitamin B12) on aptes-functionalized mesoporous silicon. *Biomed. Phys. Eng. Expr.* **2017**, *3* (5), 055007.